UNIVERSITYOF BIRMINGHAM

University of Birmingham Research at Birmingham

Asteroseismology and Gaia:

Huber, Daniel; Zinn, Joel; Bojsen-hansen, Mathias; Pinsonneault, Marc; Sahlholdt, Christian; Serenelli, Aldo; Aguirre, Victor Silva; Stassun, Keivan; Stello, Dennis; Tayar, Jamie; Bastien, Fabienne; Bedding, Timothy R.; Buchhave, Lars A.; Chaplin, William J.; Davies, Guy R.; García, Rafael A.; Latham, David W.; Mathur, Savita; Mosser, Benoit; Sharma, Sanjib

[Link to publication on Research at Birmingham portal](#)

Download date: 23. Apr. 2024

Asteroseismology and *Gaia*: Testing Scaling Relations Using 2200 *Kepler* Stars with TGAS Parallaxes

Daniel Huber[1,2,3,4], Joel Zinn[5], Mathias Bojsen-Hansen[4], Marc Pinsonneault[5], Christian Sahlholdt[4], Aldo Serenelli[6], Victor Silva Aguirre[4], Keivan Stassun[7,8], Dennis Stello[9,2,4], Jamie Tayar[5], Fabienne Bastien[10,11,18], Timothy R. Bedding[2,4], Lars A. Buchhave[12], William J. Chaplin[13,4], Guy R. Davies[13,4], Rafael A. García[14], David W. Latham[15], Savita Mathur[16], Benoit Mosser[17], and Sanjib Sharma[2]

[1] Institute for Astronomy, University of Hawai'i, 2680 Woodlawn Drive, Honolulu, HI 96822, USA; huberd@hawaii.edu
[2] Sydney Institute for Astronomy (SIfA), School of Physics, University of Sydney, NSW 2006, Australia
[3] SETI Institute, 189 Bernardo Avenue, Mountain View, CA 94043, USA
[4] Stellar Astrophysics Centre, Department of Physics and Astronomy, Aarhus University, Ny Munkegade 120, DK-8000 Aarhus C, Denmark
[5] Department of Astronomy, The Ohio State University, Columbus, OH 43210, USA
[6] Institute of Space Sciences (IEEC-CSIC), Campus UAB, Carrer de Can Magrans S/N, E-08193, Barcelona, Spain
[7] Vanderbilt University, Department of Physics and Astronomy, 6301 Stevenson Center Lane, Nashville, TN 37235, USA
[8] Fisk University, Department of Physics, 1000 17th Avenue N., Nashville, TN 37208, USA
[9] School of Physics, University of New South Wales, NSW 2052, Australia
[10] Department of Astronomy and Astrophysics, The Pennsylvania State University, 525 Davey Laboratory, University Park, PA 16802, USA
[11] Center for Exoplanets and Habitable Worlds, The Pennsylvania State University, 525 Davey Laboratory, University Park, PA 16802, USA
[12] Centre for Star and Planet Formation, Natural History Museum of Denmark & Niels Bohr Institute, University of Copenhagen, Oster Voldgade 5-7, DK-1350 Copenhagen K, Denmark
[13] School of Physics and Astronomy, University of Birmingham, Birmingham B15 2TT, UK
[14] Laboratoire AIM, CEA/DRF-CNRS, Université Paris 7 Diderot, IRFU/SAp, Centre de Saclay, F-91191, Gif-sur-Yvette, France
[15] Harvard-Smithsonian Center for Astrophysics, 60 Garden Street, Cambridge, Massachusetts 02138, USA
[16] Space Science Institute, 4750 Walnut street Suite 205, Boulder, CO 80301, USA
[17] LESIA, Observatoire de Paris, PSL Research University, CNRS, Université Pierre et Marie Curie, Université Paris Diderot, F-92195 Meudon, France
Received 2017 March 19; revised 2017 May 9; accepted 2017 May 11; published 2017 July 27

Abstract

We present a comparison of parallaxes and radii from asteroseismology and *Gaia* DR1 (TGAS) for 2200 *Kepler* stars spanning from the main sequence to the red-giant branch. We show that previously identified offsets between TGAS parallaxes and distances derived from asteroseismology and eclipsing binaries have likely been overestimated for parallaxes $\lesssim$5–10 mas ($\approx$90%–98% of the TGAS sample). The observed differences in our sample can furthermore be partially compensated by adopting a hotter $T_{\rm eff}$ scale (such as the infrared flux method) instead of spectroscopic temperatures for dwarfs and subgiants. Residual systematic differences are at the $\approx$2% level in parallax across three orders of magnitude. We use TGAS parallaxes to empirically demonstrate that asteroseismic radii are accurate to $\approx$5% or better for stars between $\approx$0.8–8 $R_\odot$. We find no significant offset for main-sequence ($\lesssim$1.5 $R_\odot$) and low-luminosity RGB stars ($\approx$3–8 $R_\odot$), but seismic radii appear to be systematically underestimated by $\approx$5% for subgiants ($\approx$1.5–3 $R_\odot$). We find no systematic errors as a function of metallicity between [Fe/H] $\approx$ −0.8 to +0.4 dex, and show tentative evidence that corrections to the scaling relation for the large frequency separation ($\Delta\nu$) improve the agreement with TGAS for RGB stars. Finally, we demonstrate that beyond $\approx$3 kpc asteroseismology will provide more precise distances than end-of-mission *Gaia* data, highlighting the synergy and complementary nature of *Gaia* and asteroseismology for studying galactic stellar populations.

Key words: parallaxes – stars: distances – stars: fundamental parameters – stars: late-type – stars: oscillations – techniques: photometric

Supporting material: machine-readable tables

1. Introduction

Over the past decade asteroseismology has emerged as an important method to systematically determine fundamental properties of stars. For example, asteroseismology has been used to determine precise radii, masses, and ages of exoplanet host stars (Christensen-Dalsgaard et al. 2010; Huber et al. 2013a; Silva Aguirre et al. 2015), calibrate spectroscopic surface gravities (Brewer et al. 2015; Petigura 2015; Wang et al. 2016), and study masses and ages of galactic stellar populations (Miglio et al. 2009; Casagrande et al. 2014b; Mathur et al. 2016; Anders et al. 2017). Due to the wealth of data from space-based missions (Chaplin & Miglio 2013) and

the complexity of modeling oscillation frequencies for evolved stars (e.g., di Mauro et al. 2011), most studies have relied on global asteroseismic observables and scaling relations to derive fundamental stellar properties. Testing the validity of these scaling relations has become one of the most active topics in asteroseismology.

Empirical tests have so far included interferometry (Huber et al. 2012; White et al. 2013), *Hipparcos* parallaxes (Miglio 2012; Silva Aguirre et al. 2012), eclipsing binaries (Frandsen et al. 2013; Huber 2015; Gaulme et al. 2016) and open clusters (Miglio et al. 2012, 2016; Stello et al. 2016). These tests have indicated that scaling relations are accurate to within $\approx$5% in radius for main-sequence stars, while larger discrepancies have been identified for giants. In particular, Gaulme et al. (2016) reported a systematic overestimation of $\approx$5% in radius and

---

[18] Hubble Fellow.

≈15% in mass for red giants with $R \gtrsim 8R_\odot$, based on a comparison with dynamical properties derived from double-lined eclipsing binaries. Semi-empirical tests using halo stars have furthermore indicated that masses from scaling relations are significantly overestimated compared to expectation values for luminous metal-poor ([Fe/H] < −1) giants (Epstein et al. 2014). Population synthesis models also suggest that the observed mass distributions are shifted toward higher masses compared to predictions (Sharma et al. 2016, 2017).

Theoretical work has motivated corrections to scaling relations, for example, by comparing the large frequency separation ($\Delta\nu$) calculated from individual frequencies with model densities (Stello et al. 2009; White et al. 2011; Guggenberger et al. 2016; Sharma et al. 2016) or an extension of the asymptotic relation (Mosser et al. 2013). A consistent result is that $\Delta\nu$ scaling relation corrections should depend on $T_{\rm eff}$, evolutionary state and metallicity. However, it is as of yet unclear whether these corrections are more important for red-giant branch or red clump stars (Miglio et al. 2012; Sharma et al. 2016). Additionally, uncertainties in modeling the driving and damping of oscillations typically prevent theoretical tests of the $\nu_{\rm max}$ scaling relation, though some studies have shown encouraging results (Belkacem et al. 2011).

Despite these efforts, the validity of scaling relations as a function of metallicity and evolutionary state is poorly tested. *Gaia* parallaxes are dramatically improving this situation by providing a large set of distances for asteroseismic samples observed by *Kepler*. Initial comparisons with *Gaia* DR1 (TGAS) using published asteroseismic distances indicated good agreement for 20 nearby dwarfs (De Ridder et al. 2016). However, subsequent work by Silva Aguirre et al. (2017) using a sample of ≈60 nearby dwarfs revealed a systematic offset between TGAS and asteroseismology, in agreement with results from eclipsing binaries by Stassun & Torres (2016b) and ground-based parallaxes for dwarfs at <25 pc (Jao et al. 2016). De Ridder et al. (2016) also found a discrepancy for ≈900 giants, which was explained as a systematic bias in TGAS parallaxes based on a comparison to red clump stars (Davies et al. 2017). Combined with the absence of offsets for distant Cepheids (Sesar et al. 2017), these results have been interpreted as evidence for a distance-dependent systematic error in TGAS parallaxes as large as ≈0.39 mas down to $\pi \approx 2$ mas (≈20%).

Here we use TGAS parallaxes for a large sample of 2200 *Kepler* stars to revisit the comparison between TGAS and asteroseismology, and to test asteroseismic scaling relations. Unlike previous studies, our sample has continuous coverage from the main sequence to the red-giant branch, allowing us to compare TGAS and asteroseismology over a range of distances and evolutionary states. A companion paper describes an investigation of correlated spatial differences between TGAS and the asteroseismic *Kepler* sample (Zinn et al. 2017).

2. Target Sample

Our sample consists of dwarfs, subgiants, and red giants from the APOGEE-Kepler Asteroseismic Science Consortium (APOKASC, Pinsonneault et al. 2014), supplemented with seismic detections using *Kepler* short-cadence data from Chaplin et al. (2014) and Huber et al. (2013b). Effective temperatures and metallicities for dwarfs and subgiants were obtained from an SPC analysis of optical high-resolution spectra obtained with the TRES spectrograph at the

F. L. Whipple Observatory (Buchhave et al. 2012, 2014). The SPC analysis was performed with externally constrained asteroseismic $\log g$ values, which prevents degeneracies between $T_{\rm eff}$, $\log g$, and [Fe/H] (Torres et al. 2012; Huber et al. 2013b). For giants, we adopted ASPCAP parameters from SDSS DR13 (Holtzman et al. 2015; SDSS Collaboration et al. 2016). We furthermore collected asteroseismic parameters $\nu_{\rm max}$ and $\Delta\nu$ from a reanalysis of the Chaplin et al. (2014) sample using all available *Kepler* data for dwarfs and subgiants (A. Serenelli et al. 2017, in preparation), and version 3.6.5 of the APOKASC catalog for giants (M. H. Pinsonneault et al. 2017, in preparation). We adopted values from the SYD pipeline (Huber et al. 2009), but note that differences between asteroseismic pipelines do not affect the conclusions in this paper (see also Section 3.3.1). Finally, we collected *griz* photometry from the *Kepler* Input Catalog (KIC, Brown et al. 2011), corrected to the SDSS scale following Pinsonneault et al. (2012), 2MASS *JHK*, Tycho $B_T V_T$, and TGAS parallaxes (Gaia Collaboration et al. 2016a, 2016b; Lindegren et al. 2016) for each star. Our final sample contains ≈440 dwarfs and subgiants as well as over 1800 red giants with asteroseismic parameters, broadband photometry, and parallaxes. Table 1 lists all observables used in this study. Unless otherwise noted, all results in this paper are based on the combination of $T_{\rm eff}$ and [Fe/H] from APOGEE and SPC, as described above.

Figure 1 shows the sample in a $T_{\rm eff}$-$\log g$ diagram, with the fractional TGAS parallax uncertainty color-coded. As expected, the fractional parallax uncertainty is a strong function of distance and hence evolutionary state: dwarfs and subgiants have a typical fractional uncerainty of ≈5%, increasing to ≈10% for subgiants and ≈50% for red clump stars. Compared to *Hipparcos*, this sample increases the number of asteroseismic *Kepler* stars with parallaxes by a factor of ≈20.

3. Methodology

3.1. Direct Method

Scaling relations for solar-like oscillations are based on the global asteroseismic observables $\nu_{\rm max}$, the frequency of maximum power, and $\Delta\nu$, the average separation of oscillation modes with the same spherical degree and consecutive radial order. The relations are defined as follows (Kjeldsen & Bedding 1995):

$$\Delta\nu \propto \left(\frac{M}{R^3}\right)^{1/2}, \tag{1}$$

$$\nu_{\rm max} \propto \frac{M}{R^2\sqrt{T_{\rm eff}}}. \tag{2}$$

Equations (1) and (2) can be rearranged to calculate radius as follows:

$$\frac{R}{R_\odot} \approx \left(\frac{\nu_{\rm max}}{\nu_{\rm max,\odot}}\right)\left(\frac{\Delta\nu}{\Delta\nu_\odot}\right)^{-2}\left(\frac{T_{\rm eff}}{T_{\rm eff,\odot}}\right)^{1/2}. \tag{3}$$

We used $\nu_{\rm max\odot} = 3090\ \mu$Hz and $\Delta\nu_\odot = 135.1\ \mu$Hz, the solar reference values for the SYD pipeline (Huber et al. 2011). Corrections for the $\Delta\nu$ scaling relation (see Section 1) were calculated using `asfgrid` (Sharma et al. 2016).[19] To calculate asteroseismic distances, we combined $T_{\rm eff}$ with the radius from Equation (3) to calculate luminosity, and then used the 2MASS

---

[19] http://www.physics.usyd.edu.au/k2gap/Asfgrid/

Table 1
Observational Data

KIC	$\nu_{max}(\mu Hz)$	$\Delta\nu(\mu Hz)$	π (mas)	B_T (mag)	V_T (mag)	g (mag)	r (mag)	i (mag)	z (mag)	J (mag)	H (mag)	K (mag)
1160789	25.221 ± 0.760	3.529 ± 0.063	1.350 ± 0.322	11.159 ± 0.051	10.059 ± 0.031	10.418 ± 0.020	9.635 ± 0.020	9.342 ± 0.020	9.195 ± 0.020	8.133 ± 0.021	7.593 ± 0.021	7.497 ± 0.017
1161618	34.363 ± 0.599	4.100 ± 0.029	1.228 ± 0.358	11.905 ± 0.101	10.657 ± 0.054	11.052 ± 0.020	10.138 ± 0.020	9.818 ± 0.020	9.652 ± 0.020	8.542 ± 0.018	7.974 ± 0.026	7.887 ± 0.018
1162746	28.042 ± 1.268	3.710 ± 0.128	0.952 ± 0.981	13.455 ± 0.392	11.815 ± 0.165	12.203 ± 0.020	11.409 ± 0.020	11.075 ± 0.020	10.878 ± 0.020	9.834 ± 0.022	9.272 ± 0.020	9.183 ± 0.018
1163621	51.170 ± 0.863	5.005 ± 0.026	0.787 ± 0.386	13.144 ± 0.331	12.044 ± 0.190	12.597 ± 0.020	11.731 ± 0.020	11.401 ± 0.020	11.188 ± 0.020	10.107 ± 0.022	9.558 ± 0.018	9.473 ± 0.018
1294385	106.498 ± 1.084	9.113 ± 0.015	1.425 ± 0.515	12.177 ± 0.156	11.027 ± 0.076	11.363 ± 0.020	10.574 ± 0.020	10.296 ± 0.020	10.139 ± 0.020	9.085 ± 0.018	8.595 ± 0.021	8.465 ± 0.018
1430163	1775.247 ± 72.128	85.873 ± 1.879	5.486 ± 0.352	10.159 ± 0.027	9.627 ± 0.023	9.694 ± 0.020	9.480 ± 0.020	9.429 ± 0.020	9.459 ± 0.020	8.769 ± 0.026	8.560 ± 0.018	8.529 ± 0.018
1433803	150.146 ± 0.997	12.179 ± 0.017	2.683 ± 0.341	11.833 ± 0.089	10.503 ± 0.046	10.967 ± 0.020	10.090 ± 0.020	9.814 ± 0.020	9.630 ± 0.020	8.538 ± 0.020	8.046 ± 0.020	7.942 ± 0.018
1435467	1382.311 ± 9.148	70.558 ± 0.053	5.598 ± 0.249	9.484 ± 0.020	9.017 ± 0.016	9.021 ± 0.020	8.778 ± 0.020	8.685 ± 0.020	8.666 ± 0.020	7.983 ± 0.024	7.753 ± 0.023	7.718 ± 0.017
1435573	25.220 ± 0.773	3.728 ± 0.091	0.636 ± 0.323	13.664 ± 0.422	11.880 ± 0.175	12.277 ± 0.020	11.338 ± 0.020	11.004 ± 0.020	10.787 ± 0.020	9.690 ± 0.021	9.150 ± 0.022	8.991 ± 0.018
1569842	134.456 ± 0.659	11.765 ± 0.017	1.246 ± 0.562	11.933 ± 0.098	11.163 ± 0.079	11.785 ± 0.020	11.010 ± 0.020	10.736 ± 0.020	10.582 ± 0.020	9.589 ± 0.022	9.074 ± 0.016	8.989 ± 0.018

Note. ν_{max} and $\Delta\nu$ were calculated using the SYD pipeline Huber et al. (2009) and taken from version 3.6.5 of the APOKASC catalog (M. H. Pinsonneault et al. 2017, in preparation) for giants and from a reanalysis of the Chaplin et al. (2014) sample for dwarfs and subgiants (A. Serenelli et al. 2017, in preparation). Note that for our analysis we added a 1% and 0.5% uncertainty in ν_{max} and $\Delta\nu$ to the formal uncertainties listed here to account for differences between asteroseismic analysis methods. $griz$ denotes KIC photometry converted into the SDSS scale using the transformations by Pinsonneault et al. (2012).

(This table is available in its entirety in machine-readable form.)

Table 2
Derived Fundamental Properties, Distances, and Extinctions

KIC	Spectroscopy + Asteroseismology			Direct Method			Direct Method ($\Delta\nu$ corr)			Grid Modeling			Grid Modeling ($\Delta\nu$ corr)			Grid Parallax			Ev	Src
	T_{eff}(K)	$\log g$	[Fe/H]	$R(R_\odot)$	d (pc)	A_V	$R(R_\odot)$	d (pc)	A_V	$R(R_\odot)$	d (pc)	A_V	$R(R_\odot)$	d (pc)	A_V	$R(R_\odot)$	d (pc)	A_V	—	—
1160789	4739 ± 86	2.307 ± 0.014	−0.340 ± 0.060	$10.84^{+0.54}_{-0.54}$	656^{+42}_{-42}	0.246	$9.85^{+0.49}_{-0.49}$	597^{+38}_{-38}	0.227	$11.29^{+0.38}_{-0.31}$	677^{+24}_{-19}	$0.133^{+0.070}_{-0.070}$	$11.29^{+0.34}_{-0.31}$	679^{+25}_{-21}	$0.133^{+0.070}_{-0.070}$	$11.92^{+7.10}_{-2.13}$	754^{+405}_{-147}	0.545	−1	apo
1161618	4763 ± 86	2.442 ± 0.009	−0.009 ± 0.060	$10.96^{+0.31}_{-0.31}$	806^{+39}_{-39}	0.085	$11.01^{+0.31}_{-0.31}$	810^{+39}_{-39}	0.086	$11.21^{+0.08}_{-0.07}$	800^{+6}_{-6}	$0.223^{+0.070}_{-0.070}$	$11.21^{+0.09}_{-0.07}$	801^{+7}_{-6}	$0.223^{+0.070}_{-0.070}$	$11.58^{+12.53}_{-2.68}$	808^{+881}_{-176}	0.108	1	apo
1162746	4798 ± 86	2.356 ± 0.020	−0.478 ± 0.060	$10.97^{+0.92}_{-0.92}$	1452^{+135}_{-135}	0.251	$10.88^{+0.92}_{-0.92}$	1441^{+134}_{-134}	0.250	$11.02^{+0.80}_{-0.58}$	1435^{+114}_{-76}	$0.353^{+0.080}_{-0.090}$	$11.02^{+0.80}_{-0.58}$	1435^{+114}_{-76}	$0.353^{+0.080}_{-0.080}$	$7.52^{+44.45}_{-2.62}$	919^{+5788}_{-399}	0.282	1	apo
1163621	4959 ± 86	2.624 ± 0.008	−0.041 ± 0.060	$11.18^{+0.29}_{-0.29}$	1722^{+79}_{-79}	0.372	$11.34^{+0.29}_{-0.29}$	1747^{+80}_{-80}	0.372	$11.10^{+0.18}_{-0.23}$	1676^{+39}_{-34}	$0.383^{+0.070}_{-0.070}$	$11.14^{+0.20}_{-0.15}$	1685^{+34}_{-27}	$0.373^{+0.080}_{-0.080}$	$8.30^{+28.31}_{-3.03}$	1216^{+4349}_{-348}	0.385	1	apo
1294385	4825 ± 86	2.936 ± 0.006	0.030 ± 0.060	$6.92^{+0.14}_{-0.14}$	667^{+29}_{-29}	0.192	$6.71^{+0.13}_{-0.13}$	646^{+28}_{-28}	0.189	$6.93^{+0.16}_{-0.12}$	668^{+17}_{-12}	$0.073^{+0.070}_{-0.070}$	$6.58^{+0.32}_{-0.12}$	633^{+31}_{-11}	$0.043^{+0.100}_{-0.090}$	$7.81^{+27.34}_{-2.19}$	754^{+2612}_{-209}	0.287	−1	apo
1430163	6590 ± 77	4.226 ± 0.018	−0.050 ± 0.101	$1.52^{+0.09}_{-0.09}$	181^{+12}_{-12}	0.057	$1.47^{+0.09}_{-0.09}$	176^{+12}_{-12}	0.056	$1.48^{+0.03}_{-0.03}$	175^{+4}_{-4}	$0.103^{+0.070}_{-0.070}$	$1.46^{+0.03}_{-0.02}$	174^{+4}_{-4}	$0.103^{+0.070}_{-0.070}$	$1.53^{+0.11}_{-0.10}$	182^{+13}_{-11}	0.057	0	spc
1433803	4721 ± 86	3.081 ± 0.005	0.198 ± 0.060	$5.41^{+0.10}_{-0.10}$	405^{+18}_{-18}	0.152	$5.23^{+0.10}_{-0.10}$	392^{+17}_{-17}	0.149	$5.38^{+0.14}_{-0.09}$	403^{+10}_{-6}	$0.083^{+0.080}_{-0.080}$	$5.14^{+0.09}_{-0.07}$	384^{+7}_{-6}	$0.053^{+0.080}_{-0.070}$	$4.97^{+0.84}_{-0.59}$	375^{+60}_{-40}	0.147	0	spc
1435467	6326 ± 77	4.108 ± 0.004	0.010 ± 0.101	$1.72^{+0.03}_{-0.03}$	138^{+5}_{-5}	0.068	$1.69^{+0.03}_{-0.03}$	136^{+5}_{-5}	0.067	$1.70^{+0.02}_{-0.02}$	137^{+2}_{-2}	$0.003^{+0.070}_{-0.070}$	$1.68^{+0.02}_{-0.01}$	135^{+2}_{-2}	$0.033^{+0.070}_{-0.080}$	$2.23^{+0.12}_{-0.12}$	177^{+9}_{-7}	0.092	0	spc
1435573	4678 ± 86	2.304 ± 0.014	0.020 ± 0.060	$9.64^{+0.58}_{-0.58}$	1156^{+83}_{-83}	0.258	$9.36^{+0.56}_{-0.56}$	1122^{+81}_{-81}	0.255	$11.09^{+0.24}_{-0.20}$	1286^{+28}_{-23}	$0.283^{+0.080}_{-0.080}$	$11.07^{+0.22}_{-0.18}$	1284^{+28}_{-20}	$0.283^{+0.080}_{-0.080}$	$12.98^{+36.18}_{-4.02}$	1470^{+4308}_{-345}	0.316	−1	apo
1569842	4847 ± 86	3.039 ± 0.004	−0.317 ± 0.060	$5.26^{+0.09}_{-0.09}$	640^{+27}_{-27}	0.291	$5.03^{+0.09}_{-0.09}$	613^{+26}_{-26}	0.283	$5.26^{+0.04}_{-0.02}$	648^{+6}_{-4}	$0.153^{+0.070}_{-0.070}$	$5.02^{+0.04}_{-0.06}$	618^{+6}_{-9}	$0.183^{+0.070}_{-0.070}$	$6.36^{+34.96}_{-1.79}$	774^{+4208}_{-216}	0.416	0	apo

Note. T_{eff} and [Fe/H] were taken from APOGEE DR13 (SDSS Collaboration et al. 2016) for giants (src flag = "apo") and from Buchhave & Latham (2015) for dwarfs and subgiants (src flag = "spc"). $\log g$ was calculated from T_{eff} and ν_{max} given in Table 1. "Ev" denotes the evolutionary state for non He-core burning stars (0), He-core burning stars (1), and stars with unknown evolutionary state (−1). Evolutionary state classifications were taken from Stello et al. (2013) and Vrard et al. (2016).

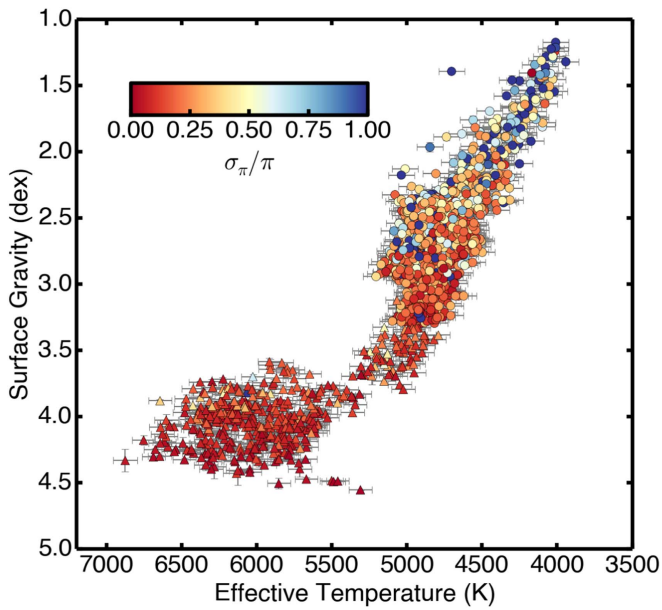(This table is available in its entirety in machine-readable form.)

Figure 1. Surface gravity vs. effective temperature for ≈1800 red giants and ≈440 dwarfs and subgiants with TGAS parallaxes and detected oscillations from *Kepler*. The fractional TGAS parallax precision is color-coded (the color scale is capped at 1 for clarity). Triangles and circles show stars with $T_{\rm eff}$ and [Fe/H] from optical (SPC, $\log g \gtrsim 3.4$) and infrared (APOGEE, $\log g \lesssim 3.4$) spectroscopy, respectively.

K-band magnitude with bolometric corrections derived by linearly interpolating $T_{\rm eff}$, $\log g$, [Fe/H], and A_V in the MIST/C3K grid (C. Conroy et al. 2017, in preparation[20]). To estimate A_V, we used the 3D reddening map by Green et al. (2015), as implemented in the `mwdust` package by Bovy et al. (2016). The derived distances, extinction values, and bolometric corrections were iterated until convergence.

Parallaxes can also be used to calculate luminosities (and hence radii), which can be compared to asteroseismic radii. To convert parallaxes into distances, we used an exponentially decreasing volume density prior with a length scale of 1.35 kpc (Bailer-Jones 2015; Astraatmadja & Bailer-Jones 2016). In practice, we implemented a Monte-Carlo method by sampling distances following the distance posterior distribution. For each distance sample, we calculated reddening given the 3D dust map, and combined this with samples for the apparent magnitude and $T_{\rm eff}$ (drawn from a random normal distribution with a standard deviation corresponding to the 1σ uncertainties) to calculate radii. The adopted bolometric corrections and $T_{\rm eff}$ values were identical to the ones used for the calculation of asteroseismic radii described above.

The resulting distributions were used to calculate the mode and 1σ confidence interval for radii derived from each *Gaia* parallax. We did not implement a more complex prior (e.g., based on a synthetic stellar population) due to the difficulty of reproducing the selection function of our sample, but note that the results in this paper do not heavily depend on the choice of distance prior.

3.2. Grid Modeling

The "direct method" for determining asteroseismic distances described in the previous section has the disadvantage that it relies on a reddening map, which may contain systematic

---

errors. We therefore calculated a second set of asteroseismic distances and TGAS radii using isochrones and synthetic photometry, which allows reddening to be treated as a free parameter. We used isochrones from the MIST database (Paxton et al. 2011, 2013, 2015; Choi et al. 2016) to calculate a grid ranging in age from 0.5 to 14 Gyr with a stepsize of 0.25 Gyr and in metallicity from −2 to +0.4 dex in stepsizes of 0.02 dex. Interpolation was performed along equal evolutionary points in age and metallicity (Dotter 2016). For each model, we saved synthetic photometry in 2MASS *JHK*, Tycho $B_T V_T$, and Sloan *griz*, and calculated reddened photometry in each passband for a given *V*-band extinction A_V by interpolating the Cardelli et al. (1989) extinction law. Asteroseismic $\nu_{\rm max}$ and $\Delta\nu$ values for each model were calculated using Equations (1) and (2), both with and without the $\Delta\nu$ scaling relation corrections by Sharma et al. (2016).

To infer model parameters, we followed the method by Serenelli et al. (2013) to integrate over all isochrone points to derive posterior distributions given a set of likelihoods and priors. Specifically, given any combination of a set of observables $x = \{B_T - V_T, \; g - r, \; r - i, \; i - z, \; J - H, \; H - K, \; \pi, \; T_{\rm eff}, \; [{\rm Fe/H}], \; \nu_{\rm max}, \; \Delta\nu\}$ and model parameters $y = \{{\rm age}, \; [{\rm Fe/H}], \; {\rm mass}, \; A_V\}$, the posterior probability is

$$p(y|x) \propto p(y)p(x|y) \propto p(y)\prod_i \, \exp\left(-\frac{(x_i - x_i(y))^2}{2\sigma_{x,i}^2}\right). \quad (4)$$

The likelihood function for π was calculated as (e.g., Bailer-Jones 2015)

$$p(\pi|d) \propto \exp\left[-\frac{1}{2\sigma_\pi^2}\left(\pi - \frac{1}{d}\right)^2\right], \quad (5)$$

where d is the model distance calculated given an absolute magnitude and A_V for each model, as well as the observed *K*-band magnitude. Probability distribution functions for each stellar parameter were then obtained by weighting $p(y|x)$ by the volume that each isochrone point encompasses in mass, age, metallicity, and A_V, and integrating the resulting distribution along a given stellar parameter (see Appendix A of Casagrande et al. 2011). For ease of computation, the integration was performed only for models within 4σ of the constraints set by the observables.

To calculate asteroseismic distances, we used as input the spectroscopic $T_{\rm eff}$ and [Fe/H], asteroseismic $\nu_{\rm max}$ and $\Delta\nu$, $B_T V_T \, griJHK$ photometry, and a flat prior in age, resulting in posterior distributions for all stellar parameters as well as extinction and distance. To calculate TGAS radii, we replaced the asteroseismic observables with the TGAS parallax π, using a flat age prior and the same distance prior as adopted in the previous section.

3.3. Validation of Seismic Distances and Gaia Radii

3.3.1. Asteroseismic Parameters

Comparisons of different methods to measure asteroseismic parameters have yielded broadly good agreement (Hekker et al. 2011, 2012; Verner et al. 2011). The median scatter between the five methods in the APOKASC catalog (see Pinsonneault et al. 2014) is 0.5% in $\Delta\nu$ and 1% in $\nu_{\rm max}$, which we added in quadrature to the formal uncertainties from the SYD pipeline (see Table 1) for the analysis described in the previous section.
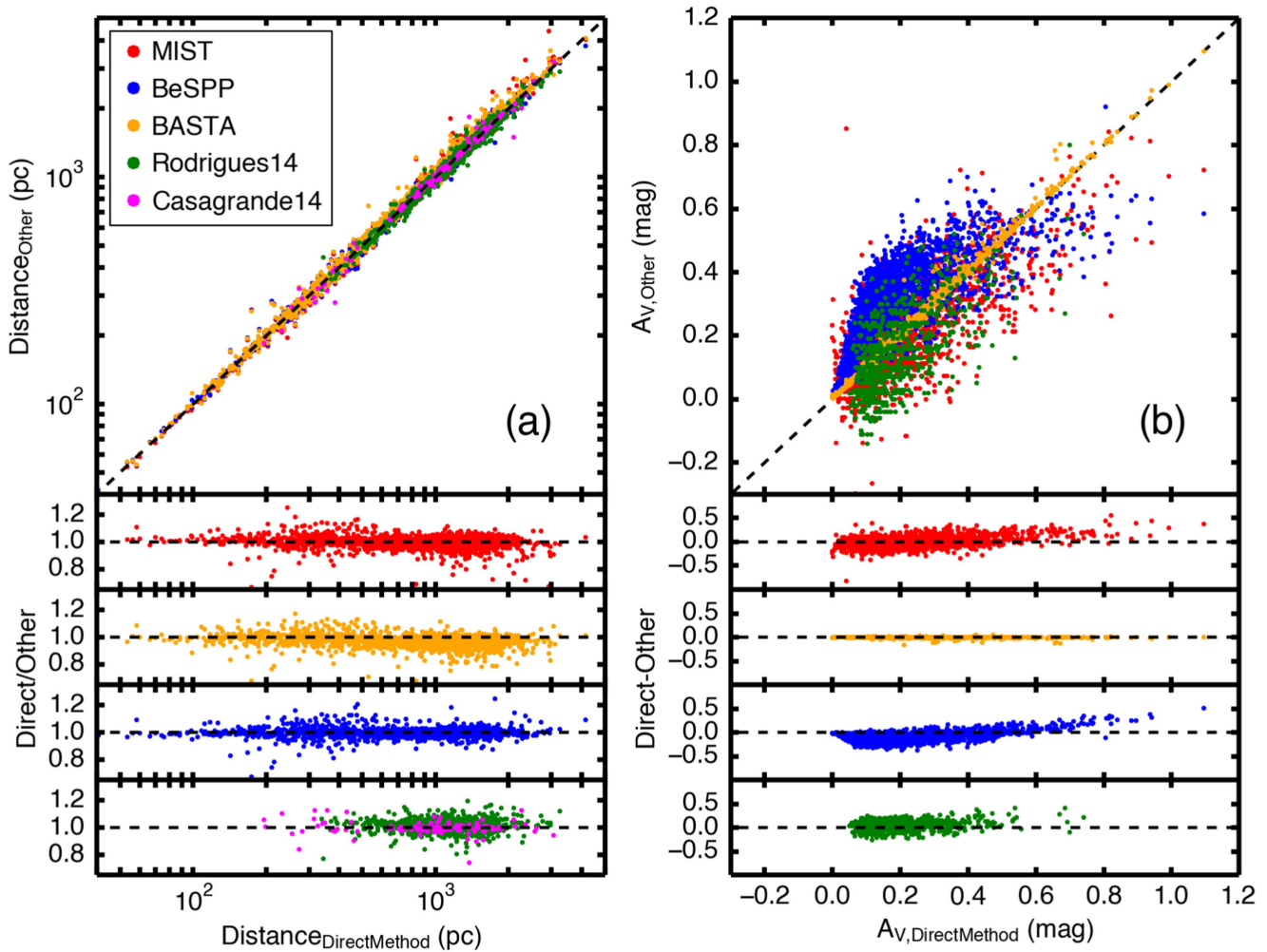
Figure 2. Panel (a): comparison of asteroseismic distances from the direct method with grid-modeled distances derived using MIST (this work), BeSPP (Serenelli et al. 2013), BASTA (Silva Aguirre et al. 2015), as well as values from the SAGA survey (Casagrande et al. 2014b) and Rodrigues et al. (2014). The top panel shows the 1:1 relation, and the bottom panels show residuals. Panel (b): comparison of extinction values from the 3D map by Green et al. (2015) (as applied in the direct method) with values derived by combining asteroseismology, spectroscopy, and photometry (MIST and Rodrigues et al. 2014) and the extinction model by Amôres & Lépine (2005; as applied in BeSPP). Colors mark the same data sets as in panel (a). Note that BASTA uses the same reddening map as the direct method in this work.

To test the influence of systematic errors, we compared our asteroseismic distances calculated using the direct and grid-modeling method in Figure 2(a). The agreement is excellent, with a median offset of 0.2% and scatter of 2.6%. To test a variety of systematic errors that could enter the asteroseismic distance calculation, we compared our distances from the direct method with distances calculated using the Bellaterra Stellar Properties Pipeline (BeSPP, Serenelli et al. 2013), the BAyesian STellar Algorithm (BASTA, Silva Aguirre et al. 2015), as well as to literature values from the Stromgren Survey for Asteroseismology and Galactic Archeology (SAGA, Casagrande et al. 2014b) and Rodrigues et al. (2014). Three of these methods (BeSPP, BASTA, SAGA) used asteroseismic input values from the same pipeline but different isochrone grids, and one method used different asteroseismic input values and isochrone models (Rodrigues et al. 2014). The median offsets are ≈0.2% for BeSPP, 2.3% for BASTA, 0.1% for SAGA, and 1.8% for Rodrigues et al. (2014), with no strong systematic trends as a function of distance (see bottom panel of Figure 2(a)). We thus conclude that systematic differences between asteroseismic methods to calculate distances are of the order of a few percent.

3.3.2. Extinction

Asteroseismic distances rely on extinction corrections, which can introduce systematic errors. Figure 2(b) compares the extinction measured using our grid-based method with the reddening map by Green et al. (2015), as applied in our direct method. We also show extinctions from Rodrigues et al. (2014), which were derived in a similar manner to the grid-modeling estimates presented here, and values from the model by Amôres & Lépine (2005), as applied by the BeSPP pipeline. The estimates agree well for $A_V \lesssim 0.5$ mag, with a slight systematic overestimation by up to 0.2 mag of the Green et al. (2015) reddening map for $A_V \gtrsim 0.5$ mag. This comparison demonstrates that the combination of spectroscopy, asteroseismology, and *Gaia* has strong potential for constructing empirical 3D reddening maps, in particular, when combined with asteroseismic detections in different regions of the galaxy as provided by CoRoT (Hekker et al. 2009) and K2 (Stello et al. 2017).

We note that the slight bias for high extinction in Figure 2(b) has only a small effect on Figure 2(a), since the sample is dominated by stars with low extinction. Additionally, a systematic shift of 0.2 mag in A_V corresponds to an error of
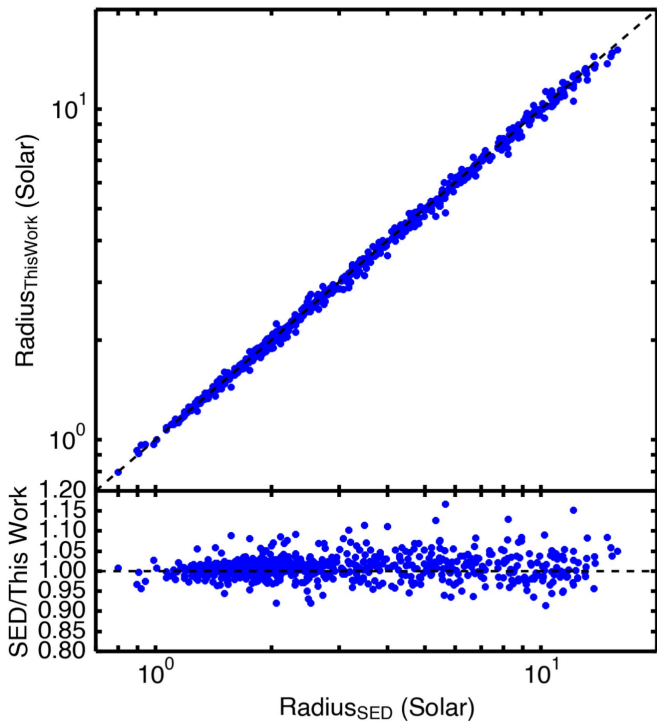
Figure 3. Comparison between radii calculated from TGAS parallaxes and bolometric corrections adopted from the MIST/C3K grid vs. bolometric fluxes measured using SED fitting as described in Stassun & Torres (2016a). The black dashed line shows the 1:1 relation.

0.02 mag in A_K, or $\lesssim 1\%$ in distance. Since distances from the direct method are the least model-dependent and more directly test the validity of scaling relations, we proceed with using these values for the remainder of the paper. We note that our main conclusions are independent of whether the direct method or the grid-modeling method is adopted.

3.3.3. Bolometric Corrections

To test the effect of systematic errors in bolometric corrections, we used the method by Stassun & Torres (2016a) to calculate bolometric fluxes by fitting spectral energy distributions to broadband photometry supplemented with a grid of ATLAS model atmospheres (Kurucz 1993). The SED fits used the same $T_{\rm eff}$, $\log g$, and [Fe/H] values as input constraints, but reddening was left as a free parameter. We then used these bolometric fluxes with $T_{\rm eff}$ to calculate angular diameters which, combined with TGAS parallaxes, resulted in a set of stellar radii that could be directly compared with the radii calculated from TGAS parallaxes and bolometric corrections (see Section 3.1). Figure 3 shows a comparison between the two estimates. We observe good agreement, with a median difference of 0.7% and a scatter of $\approx 3\%$, and a small systematic trend with SED radii being larger by $\approx 1\%$ for red giants (≈ 3–$10\,R_\odot$).

Since the MIST grid also uses ATLAS models, the above exercise is mostly sensitive to differences in deriving bolometric fluxes rather than systematic differences in model atmospheres. We therefore performed a second test by comparing distances calculated using the same seismic luminosity and reddening but bolometric corrections calculated from MARCS model atmospheres (Gustafsson et al. 2008) provided by Casagrande & VandenBerg (2014), as implemented in BASTA (see also

the left panel of Figure 2). We observed an offset of $\approx 1\%$ (with distances calculated using MARCS bolometric corrections being larger), which was approximately constant in distance. Based on these two tests, we conclude that systematic errors due to bolometric corrections are at the $\approx 1\%$ level in radius and distance, which is small compared to the random uncertainties of TGAS parallaxes (see Figure 1).

3.4. Code Availability

The stellar classification software tools described above as well as all data to reproduce the results of this paper (Tables 1 and 2) are publicly available at https://github.com/danxhuber/isoclassify (Huber 2017). The tools can be used to derive posterior distributions for stellar parameters and distances given any input combination of asteroseismic, astrometric, photometric, and spectroscopic observables.

4. Results

4.1. Parallax Comparison

Figure 4 compares parallaxes from asteroseismology with those from TGAS for all 2200 stars in our sample. We show results without $\Delta\nu$ correction applied, but note that the effects of this correction are small compared to the scatter (see Section 4.2). Qualitatively, the comparison shows good agreement over three orders of magnitude. The scatter is dominated by large TGAS uncertainties for distant, evolved stars, which cause a diagonal "edge" in the ratios (bottom panel) toward low parallax values due to TGAS data systematically scattering to lower values than asteroseismology. This is mainly caused by asteroseismic distances being an order of magnitude more precise: because the giant sample is magnitude limited, we observe a lack of small parallax values from asteroseismology.

The qualitative agreement in Figure 4 appears to contradict De Ridder et al. (2016), who reported that asteroseismic and TGAS parallaxes are incompatible with a 1:1 relation for ≈ 900 giants from Rodrigues et al. (2014). To investigate this, we compare stars with parallaxes <5 mas (corresponding roughly to the largest parallax in the sample by Rodrigues et al. 2014) on a linear scale in Figure 5. We indeed observe a deviation from the 1:1 relation, with seismic parallaxes being systematically larger. However, the larger sample used here, which covers the transition from red giants to main-sequence stars (Figure 1), demonstrates that this deviation appears to be significantly smaller than previously thought. Specifically, the TGAS parallax corrections derived from eclipsing binaries by Stassun & Torres (2016b), which indicated that TGAS parallaxes are too small ($\pi_{\rm TGAS-EB} = -0.25$ mas using the mean offset or $\pi_{\rm TGAS-EB} = -0.39$ mas using an ecliptic latitude $\beta = 55°$) are significantly too large. There is also tension with the upper end of the Davies et al. (2017) correction (which predicts a similar offset to Stassun & Torres 2016b at ≈ 1.6 mas). We note that these results are not significantly affected by the small offset between our distances and Rodrigues et al. (2014) discussed in Section 3.3.1.

In agreement with the combined results by Sesar et al. (2017), Jao et al. (2016), and Davies et al. (2017), we find that the absolute offset increases for larger parallaxes, which, on average, correspond to less evolved stars. This implies a stronger absolute systematic offset for main-sequence stars and subgiants, which is surprising given that scaling relations are
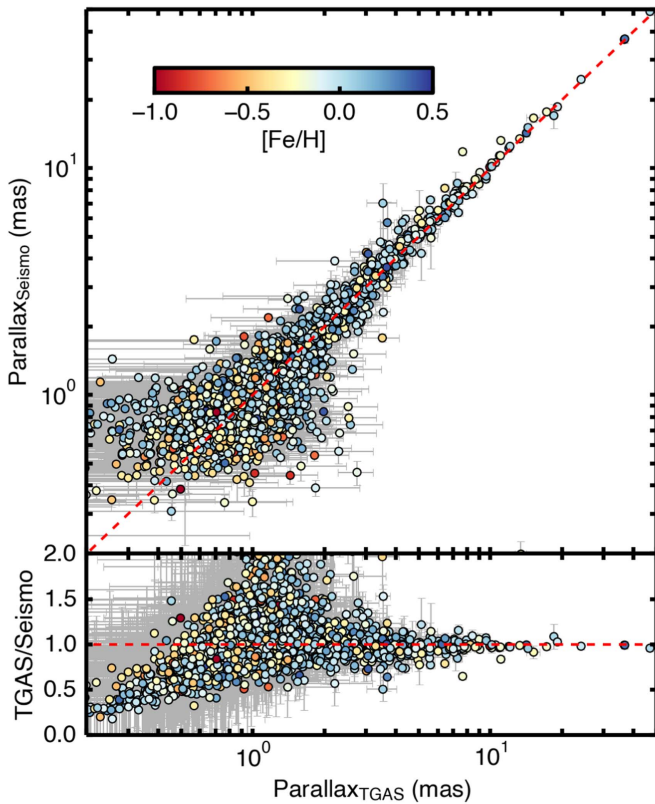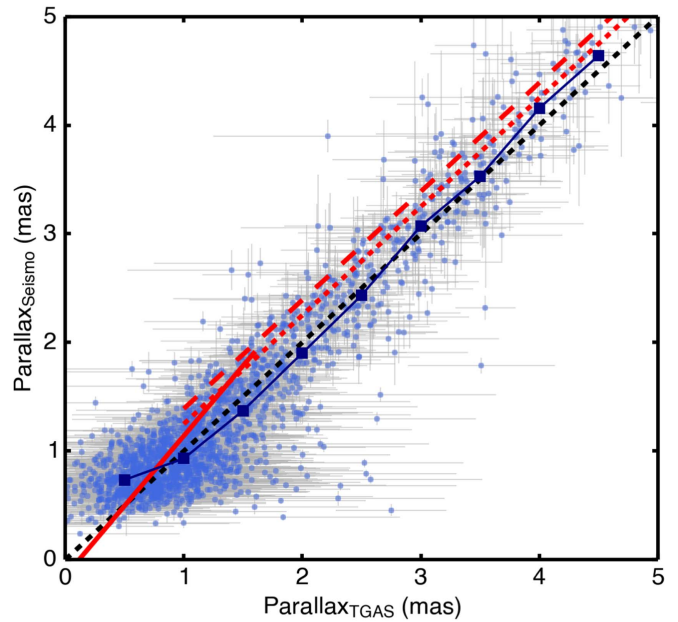
Figure 5. Asteroseismic vs. TGAS parallaxes for stars with $\pi < 5$ mas. The dashed black line shows the 1:1 relation. Light blue symbols are individual stars, while thick dark blue squares show median bins spaced by 0.5 mas. The red dashed and dotted lines show the predicted offsets from the TGAS parallax corrections by Stassun & Torres (2016b) with and without ecliptic latitude dependence, respectively. The solid red line shows the predicted offset from the TGAS parallax correction by Davies et al. (2017).

Figure 4. Asteroseismic parallaxes (calculated using the direct method without $\Delta\nu$ correction) vs. TGAS parallaxes for all 2200 stars in our sample. Metallicities are color-coded, and the dashed red line shows the 1:1 relation.

generally thought to be more reliable for stars similar to the Sun. However, asteroseismic distances scale as $T_{\rm eff}{}^{2.5}$, which varies significantly for main-sequence and subgiant stars. Indeed, $T_{\rm eff}$ scales are often plagued by systematic offsets (e.g., Pinsonneault et al. 2012). In general, photometric $T_{\rm eff}$ scales from the infrared flux method (Casagrande et al. 2011) or open clusters (An et al. 2013) are systematically hotter than spectroscopic temperatures, though recent color-$T_{\rm eff}$ calibrations are consistent with or cooler than spectroscopy (Huang et al. 2015). All $T_{\rm eff}$ scales rely on the accuracy of interferometric angular diameters (e.g., Boyajian et al. 2012a, 2012b; White et al. 2013), some of which have been suspected to be affected by systematic errors (Casagrande et al. 2014a). While efforts to systematically cross-calibrate angular diameters between different instruments are currently underway (e.g., Huber 2016), it is still unclear which $T_{\rm eff}$ scale is indeed most accurate.

To test the effect of changing the $T_{\rm eff}$ scale, we recalculated asteroseismic distances for dwarfs and subgiants using temperatures from the APOGEE pipeline (ASPCAP), and also using photometric $T_{\rm eff}$ values from the infrared flux method (IRFM, Casagrande et al. 2011) and Sloan photometry (SDSS, Pinsonneault et al. 2012) as listed in Pinsonneault et al. (2012). We note that that Pinsonneault et al. (2012) used [Fe/H] = -0.2 dex and extinction values from the KIC, which were shown to be overestimated compared to values derived from asteroseismology and spectroscopy (Rodrigues et al. 2014). Accounting for these differences would result in shifts of ≈ -20 K for the SDSS and ≈ -65 K for the IRFM scales, depending on the adopted initial $T_{\rm eff}$ and extinctions. Furthermore, the SDSS and IRFM scales are not entirely independent, since SDSS was calibrated to match

IRFM for $T_{\rm eff} > 6000$ K. Re-deriving the SDSS and IRFM $T_{\rm eff}$ scales for the sample is beyond the scope of this paper, but we note that neither of these effects significantly change the conclusions below.

For comparison, we discarded stars with $\pi < 1.5$ mas to avoid the "edge" bias that arises from large uncertainty differences discussed above. The average difference between the coolest (ASPCAP) and hottest (IRFM) $T_{\rm eff}$ scale is ≈ 270 K. The results in Figure 6 demonstrate that the hotter $T_{\rm eff}$ scales bring better agreement between asteroseismic and TGAS parallaxes, particularly for $\pi \lesssim 10$ mas. Specifically, the median offset over the whole sample reduces by more than a factor of 2 from $5.8 \pm 0.6\%$ for the coolest $T_{\rm eff}$ scale (ASPCAP) to $2.0 \pm 0.7\%$ for the IRFM. Figure 6 also shows the proposed corrections by Stassun & Torres (2016b) derived from eclipsing binaries. The -0.25 mas correction, which was the main result of the study, provides a good match to the data for $\pi \gtrsim 5$ mas and spectroscopic $T_{\rm eff}$ scales, but is overestimated for $\pi \lesssim 5$ mas for all $T_{\rm eff}$ scales. The correction including an ecliptic latitude dependence is overestimated for $\pi \lesssim 10$ mas for all $T_{\rm eff}$ scales.

In summary, our analysis demonstrates that offsets between TGAS parallaxes, asteroseismology, and eclipsing binaries are likely smaller than previously reported for $\pi \lesssim 5$–10 mas ($\gtrsim 100$–200 pc), and can be at least partially compensated by systematic errors in $T_{\rm eff}$ scales for dwarfs and subgiants. Residual differences are small fractions rather than absolute offsets, and are $\approx 2\%$ for the hottest $T_{\rm eff}$ scales. This conclusion is consistent with Silva Aguirre et al. (2017) and Jao et al. (2016), who found agreement with the offset by Stassun & Torres (2016b) for nearby dwarfs for which $\approx 2\%$ produces a -0.25 mas offset. These results imply that previously proposed TGAS parallax corrections are overestimated for $\pi \lesssim 5$–10
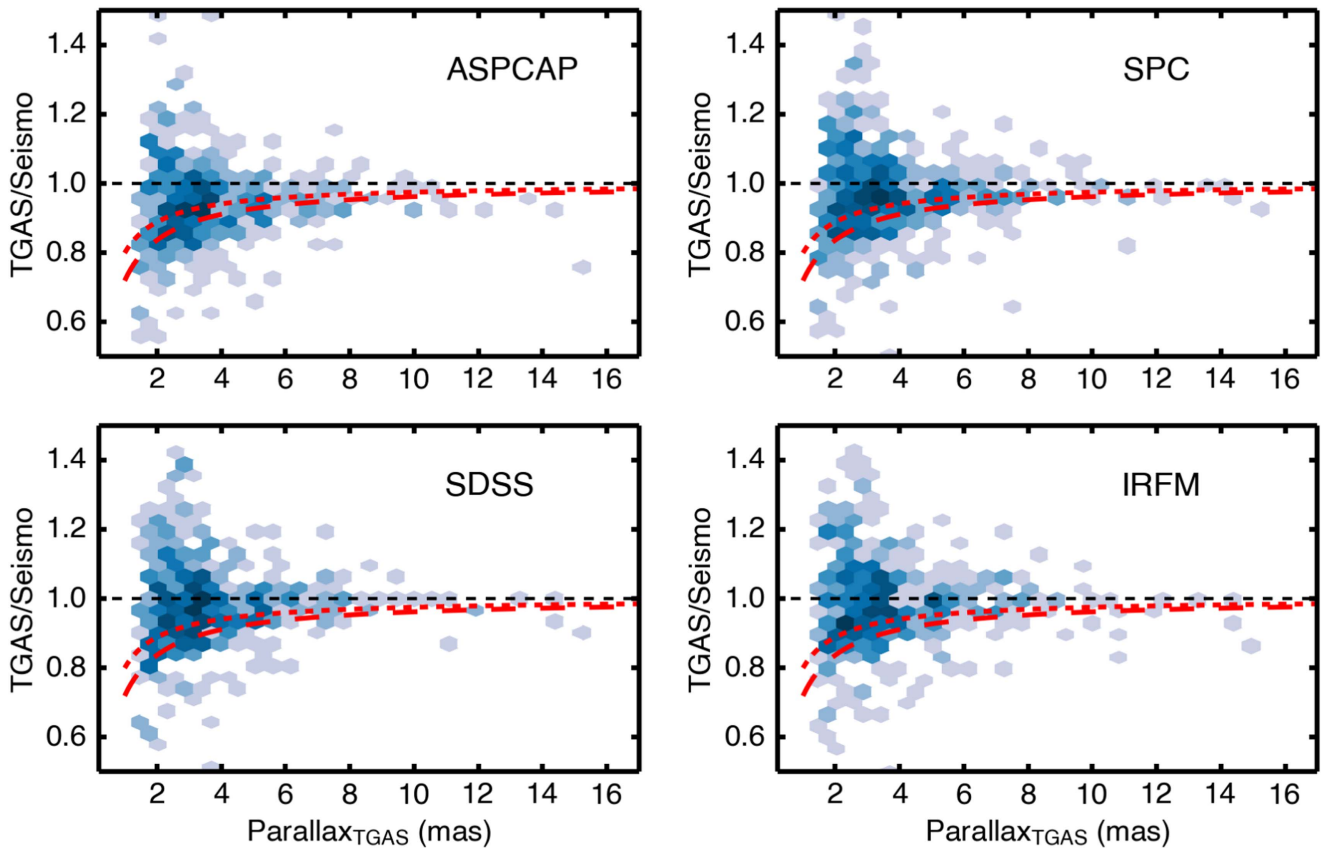
Figure 6. Ratio of asteroseismic and TGAS parallaxes as a function of TGAS parallax for the dwarf and subgiant sample with $\pi > 1.5$ mas. Colors show the logarithmic number density, with darker colors corresponding to a higher number of stars. Each panel shows a different adopted $T_{\rm eff}$ scale to calculate asteroseismic parallaxes. The average temperature offsets are $\Delta(T_{\rm eff})_{\rm SDSS-ASPCAP} \approx 220$ K, $\Delta(T_{\rm eff})_{\rm IRFM-ASPCAP} \approx 270$ K, $\Delta(T_{\rm eff})_{\rm SDSS-SPC} \approx 110$ K, and $\Delta(T_{\rm eff})_{\rm IRFM-SPC} \approx 140$ K. We note that ASPCAP temperatures are not calibrated for dwarfs (Holtzman et al. 2015), and hence are likely underestimated. The red dashed and dotted lines show the predicted offsets from the TGAS parallax corrections by Stassun & Torres (2016b) with and without ecliptic latitude dependence, respectively.

mas ($\approx$90%–98% of the TGAS sample). We note that this difference is most likely due to the larger sample size used in this study, rather than systematic differences in the adopted methods or distance scales. The above results also provide empirical evidence that hotter $T_{\rm eff}$ scales (such as the infrared flux method) are more accurate than cooler, spectroscopic estimates. Importantly, this conclusion assumes that there are no strong systematic errors in TGAS and asteroseismic distances.

4.2. Radius Comparison

Comparing radii instead of parallaxes reduces the $T_{\rm eff}$ dependence (from $T_{\rm eff}^{2.5}$ to $T_{\rm eff}^{1.5}$) and allows a more direct test of a fundamental parameter predicted by scaling relations. Figure 7 compares asteroseismic and TGAS radii for all stars with a TGAS parallax measured to better than 20%, which approximately corresponds to the limit where the distance ratios are not heavily influenced by the exponentially decreasing volume density prior (see Section 3.1) or artifacts introduced by large differences in random errors (see Section 4.1). The overall agreement is excellent, empirically demonstrating that asteroseismic radii from scaling relations without any corrections are accurate to at least $\approx$10% for stars ranging from $\approx$0.8 to 10 $R_\odot$. The color-coding in Figure 7 furthermore demonstrates that there are no strong biases in asteroseismic radii as a function of metallicity.

To illustrate this further, Figure 8 shows the ratios as a function of $T_{\rm eff}$, $\log g$, [Fe/H], and TGAS radius, both with and without applying the $\Delta\nu$ correction by Sharma et al. (2016). In addition to the raw data (small symbols), we also show median bins (large symbols). We have tested that spatial correlations between asteroseismic and TGAS parallaxes (Zinn et al. 2017) do not significantly affect these median values or their uncertainties for the typical spatial separations of stars contributing to a given bin ($\approx$1°5). We also show 68% confidence intervals calculated by bootstrapping a local-quadratic nonparametric regression using `pyqt-fit`.[21]

We observe no significant trends with metallicity for [Fe/H] = −0.8 to +0.4 dex (Figure 8(b)). Intriguingly, however, the ratios show a trend as a function of TGAS radius (Figure 8(d)): stars near the main sequence ($\sim$1–1.5 $R_\odot$) show no offset, while the seismic radii of subgiants ($\sim$1.5–3 $R_\odot$) are too small by $\approx$5%–7%. The offset reduces for low-luminosity red giants, before increasing for high-luminosity red giants ($\gtrsim 10 R_\odot$). The $\Delta\nu$ scaling relation correction slightly reduces these deviations (blue triangles). The upturn for high-luminosity red giants ($\gtrsim 10 R_\odot$) in Figure 8(d) is artificially introduced by large uncertainties of TGAS radii in a magnitude-limited sample, similar to the "edge" bias for parallaxes in the bottom panel of Figure 4. The underestimated seismic radii for subgiants, however, cannot be explained by such an effect.
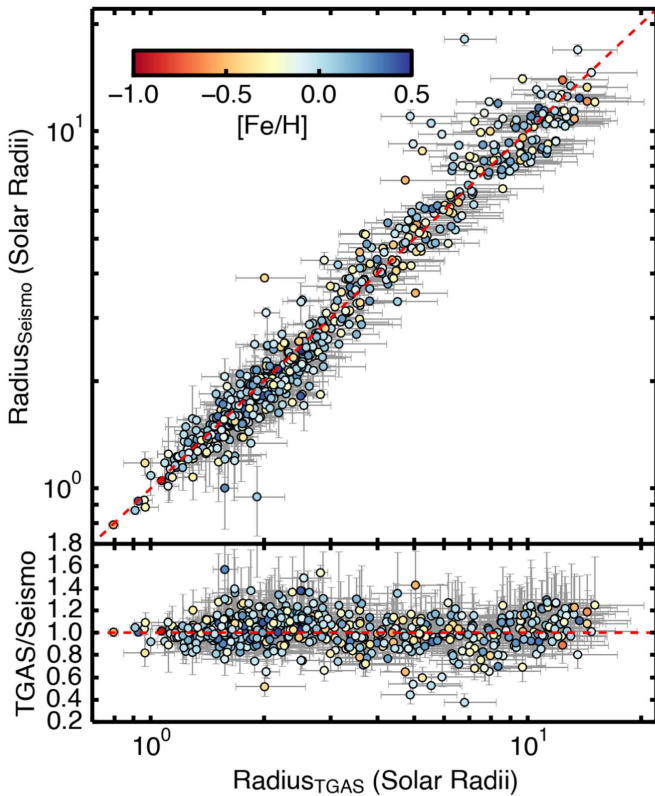
---

[21] http://pyqt-fit.readthedocs.io/en/latest/modules.html

Figure 7. Comparison of radii derived using TGAS parallaxes with radii calculated from asteroseismic scaling relations for stars with $\sigma_\pi/\pi < 0.2$. No $\Delta\nu$ correction was applied. Color-coding denotes the metallicity for each star. The average residual median and scatter is ~3% and ~10%, respectively.

We confirmed that the radius trend in Figure 8(d) is independent of the distance prior, reddening, method for calculating asteroseismic observables, or adopted $T_{\rm eff}$ scales (see Figure 9). Note that we have excluded giants with $R > 10 R_\odot$ from this comparison to remove the bias discussed above. Specifically, we used a flat distance prior, reddening measured from the grid-modeling method described in Section 3.2, as well as $\nu_{\rm max}$ and $\Delta\nu$ values from the COR pipeline (Mosser & Appourchaux 2009). Adopting IRFM $T_{\rm eff}$ values for dwarfs and subgiants instead of the default SPC scale reduced the offset for subgiants by ≈2% (magenta symbols Figure 9). We added this value in quadrature in the subsequent analysis to account for $T_{\rm eff}$-dependent systematics.

To put the TGAS radius comparison into context, Figure 10 also shows results from eclipsing binaries (Gaulme et al. 2016) and interferometry (Huber et al. 2012; White et al. 2013; Johnson et al. 2014). The interferometry sample is sparse for subgiants, but does not strongly contradict the ≈5% bias for subgiants from TGAS. For giants, our results are compatible with Gaulme et al. (2016), though the $\Delta\nu$-corrected results are in slight tension with their predicted 5% offset. Either way, the TGAS results imply that the ≈5% radius bias reported by Gaulme et al. (2016) does not seem to extend the regime of low-luminosity red giants, which are prime targets for studies of exoplanets orbiting asteroseismic hosts (Grunblatt et al. 2016). A larger interferometric sample (T. R. White et al. 2017, in preparation) as well as spectrophotometric angular diameters in combination with *Gaia* parallaxes (S. K. Grunblatt et al. 2017, in preparation) will allow us to confirm and quantify the trends in Figure 10. Table 3 lists the median binned ratios

shown in Figure 10, which may be used to estimate systematic errors in seismic radii from scaling relations.

4.3. Red-giant Branch versus Red Clump

Models of red giants lead us to expect a systematic difference in the $\Delta\nu$ scaling relation as a function of the evolutionary state due to the changes in their interior sound-speed profile after the onset of He-core burning (Miglio et al. 2012). However, the degree and even the sign of this difference is not yet fully settled. For example, Miglio et al. (2012) showed that applying the $\Delta\nu$ correction to red clump stars improves the agreement with independent radii measured in clusters, while the results by Sharma et al. (2016) implied that the largest effect of the $\Delta\nu$ correction applies for ascending RGB stars. Previous samples to empirically test scaling relations have been too small to decide this question.

TGAS parallaxes allow us to test the dependency of the scaling relation correction on evolutionary state. To separate RGB and red clump stars, we used classifications based on mixed mode period spacings by Stello et al. (2013) and Vrard et al. (2016). Figure 11 shows parallaxes (left panels) and radii (right panels) both with (bottom) and without (top) applying the $\Delta\nu$ scaling relation correction by Sharma et al. (2016). The samples in each panel are separated into RGB (blue circles) and red clump stars (red triangles). Note that we relaxed the fractional parallax uncertainty cut to <40% to include more red clump stars in the sample. Due to this relaxed cut, the median bins were offset from the local-quadratic fit, and we thus adopted mean bins for consistency. However, the conclusions below are not unaffected by whether mean or median bins are used.

While the scatter is too large to determine whether the RGB or red clump stars agree better with TGAS, there is tentative evidence that the $\Delta\nu$ correction provides a improvement for RGB stars. Specifically, the weighted mean offset reduces from 5.4 ± 1.3% to 2.7 ± 0.7% in parallax and from −3.1 ± 1.4% to −1.0 ± 1.5% for radius. The corrections for red clump stars are negligible, as expected. We conclude that TGAS parallaxes are not precise enough to decide how the $\Delta\nu$ correction depends on evolutionary state, but provide tentative evidence (at the ≈2σ level) that the Sharma et al. (2016) corrections improve the accuracy of seismic distances and radii.

4.4. Synergies of Gaia and Asteroseismic Distances

TGAS provides a first glimpse of the potential of *Gaia* to measure distances, and vast precision improvements are expected for upcoming data releases. Since asteroseismic and TGAS distances agree to within a few percent over several orders of magnitude, it is interesting to explore the complementary nature of *Gaia* and asteroseismology to measure distances to galactic stellar populations. To investigate this, we calculated the expected end-of-mission *Gaia* parallax precision for seismic *Kepler* targets using the *Gaia* performance model:[22]

$$\sigma_\pi/{\rm mas} = \sqrt{(-1.631 + 680.766z + 32.732z^2)} \\ \times (0.986 + (1 - 0.986)V - I_C), \qquad (6)$$
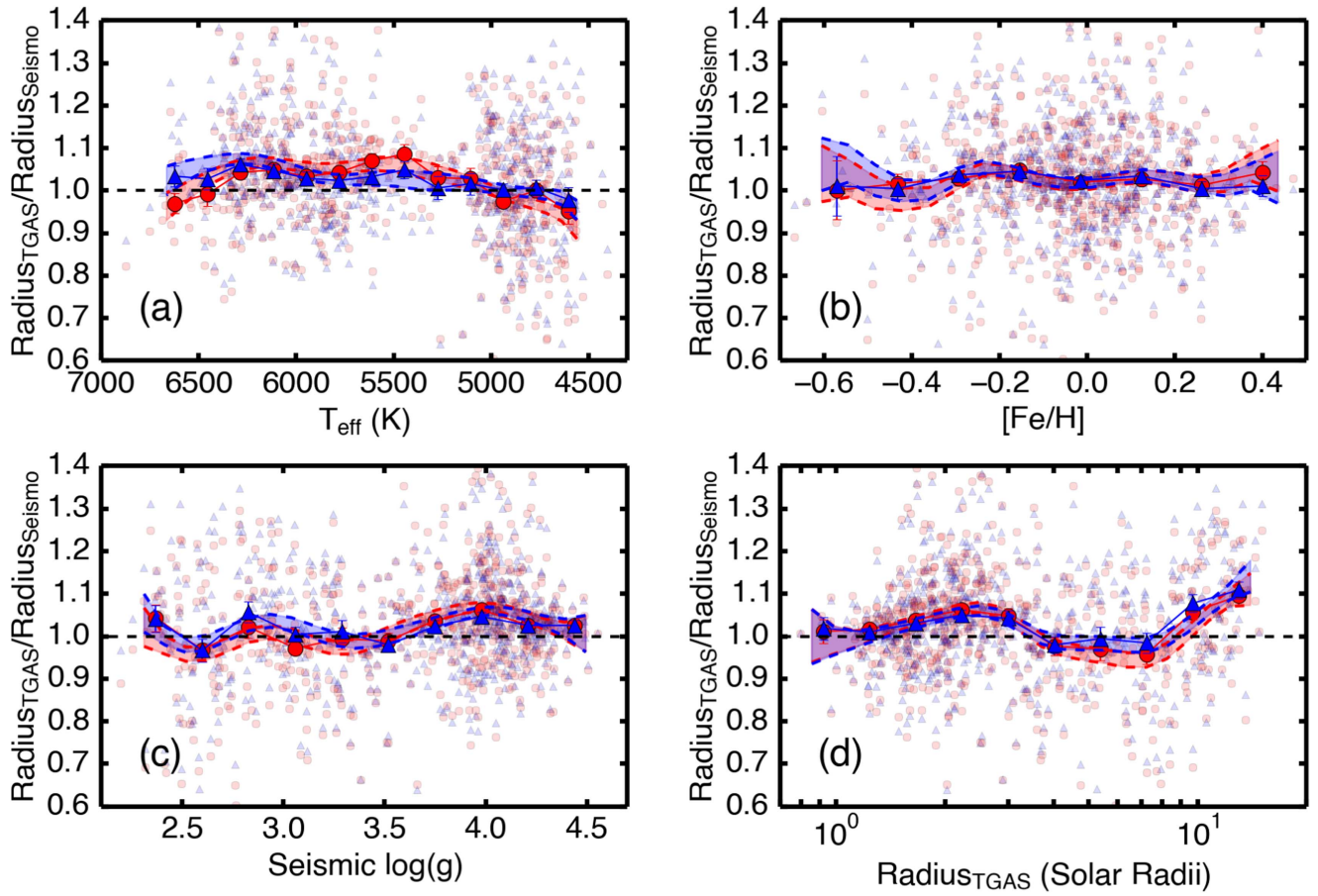
---

[22] http://www.cosmos.esa.int/web/gaia/science-performance

Figure 8. Ratio of TGAS radii over asteroseismic radii as a function of $T_{\rm eff}$, $\log g$ [Fe/H], and TGAS radius. Small red circles and blue triangles show unbinned data with and without applying the Sharma et al. (2016) $\Delta\nu$ scaling relation correction, respectively. Thick symbols show median binned data. Shaded areas and dashed lines show 68% confidence intervals calculated by bootstrapping a local-quadratic nonparametric regression using pyqt-fit. Note that the upturn for large radii is an artifact due to the large uncertainty differences between both samples (see the text and Figure 10).
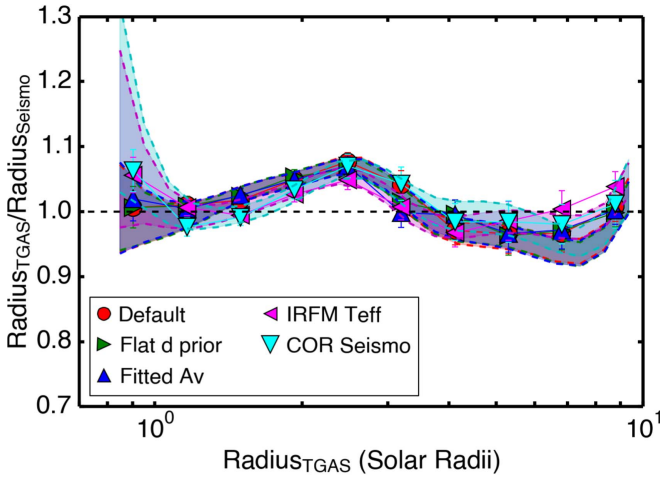
Figure 9. Same as Figure 8(d) but restricting the sample to stars with $R < 10\,R_\odot$ and only showing results using no $\Delta\nu$ correction (red circles). Different symbols and colors show the same analysis repeated assuming a flat distance prior (green right-facing triangles), using reddening values measured using grid-modeling (blue upwards triangles), using IRFM temperatures (magenta left-facing triangles), and using seismic parameters from the COR pipeline (cyan downwards triangles). Note that the large uncertainties at the lowest radii are caused by the sparseness of cool dwarfs in some of the test samples.
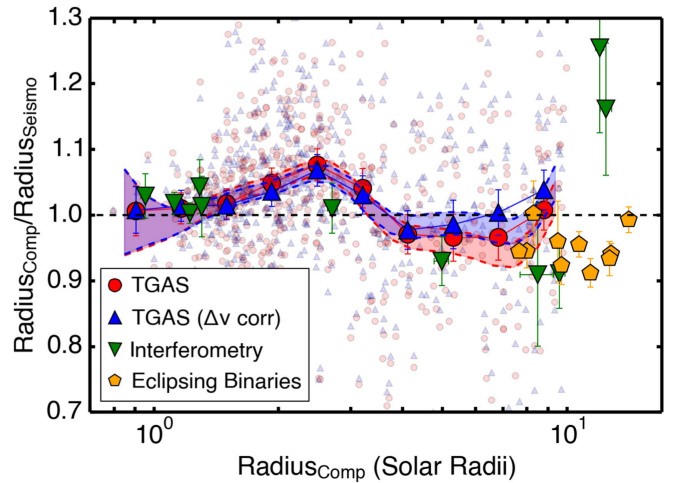
Figure 10. Comparison of asteroseismic radii derived from scaling relations with radii derived from four methods. Red circles and blue upward triangles show our TGAS sample with and without the Sharma et al. (2016) $\Delta\nu$ scaling relation correction, and shaded areas show 68% confidence intervals as in Figure 8. We also show stars with interferometrically measured radii (green triangles, Huber et al. 2012; White et al. 2013; Johnson et al. 2014) and red giants in double-lined eclipsing binary systems (orange pentagons, Gaulme et al. 2016).

Table 3
Median Binned Ratios between *Gaia* and Seismic Radii

$R_{\rm Gaia}(R_\odot)$	$R_{\rm Gaia}/R_{\rm seismo}$	$R_{\rm Gaia}/R_{\rm seismo,\Delta\nu corr}$
0.90	1.007 ± 0.038	1.008 ± 0.035
1.16	1.010 ± 0.024	1.014 ± 0.024
1.50	1.018 ± 0.023	1.015 ± 0.022
1.93	1.049 ± 0.023	1.036 ± 0.023
2.48	1.077 ± 0.024	1.069 ± 0.024
3.20	1.041 ± 0.030	1.031 ± 0.029
4.12	0.971 ± 0.030	0.977 ± 0.029
5.30	0.966 ± 0.036	0.986 ± 0.037
6.83	0.966 ± 0.035	1.004 ± 0.035
8.79	1.008 ± 0.030	1.039 ± 0.030

Note. $R_{\rm seismo,\Delta\nu corr}$ corresponds to seismic radii derived using the $\Delta\nu$ scaling relation correction by Sharma et al. (2016; i.e., blue symbols in Figure 10). Uncertainties include a 2% systematic error due to different $T_{\rm eff}$ scales.

with

$$z = \begin{cases} 0.0685 & \text{for } G < 12.1 \\ 10^{0.4(G-15)} & \text{otherwise} \end{cases} \quad (7)$$

Here, σ_π is the predicted end-of-mission parallax uncertainty averaged over the sky. The *Gaia* G-band magnitude and Johnson-Cousins $V - I$ color were calculated from KIC *gri* photometry (Table 1) using the following relations (Jordi et al. 2006, 2010):

$$G = (-0.0662 - 0.7854(g - r) - 0.2859(g - r)^2 + 0.0145(g - r)^3) + g, \quad (8)$$

and

$$V - I = \begin{cases} 0.675(g - r) + 0.364 & \text{for } g - r < 2.1 \\ 1.11(g - r) - 0.52 & \text{otherwise.} \end{cases} \quad (9)$$

To account for the sky-position dependency of parallax uncertainties due to the *Gaia* scanning law, we interpolated the recommended scaling factors[23] for the ecliptic coordinates of each *Kepler* target. This yielded on average ~28% smaller uncertainty than the uncertainties calculated from Equation (6).

Figure 12 compares the distance uncertainty from asteroseismology to the expected end-of-mission *Gaia* precision for stars with asteroseismic distances from this work, Rodrigues et al. (2014), Casagrande et al. (2014b), and Mathur et al. (2016).[24] Remarkably, asteroseismology will provide more precise distances than the best *Gaia* performance for stars beyond 3 kpc. This is because the asteroseismic sensitivity does not depend strongly on apparent magnitude and hence distant, high-luminosity red giants still yield precisions of a few percent out to tens of kiloparsecs (Mathur et al. 2016). Asteroseismology will therefore be critical to extend the reach of *Gaia* to distant stellar populations, particularly if combined with spectroscopy, which simultaneously allows us to constrain interstellar extinction (Figure 2). Current and future opportunities to detect oscillations in distant red giants outside the *Kepler* field include the K2 Mission (Howell et al. 2014), targets with one-year coverage near the ecliptic poles observed
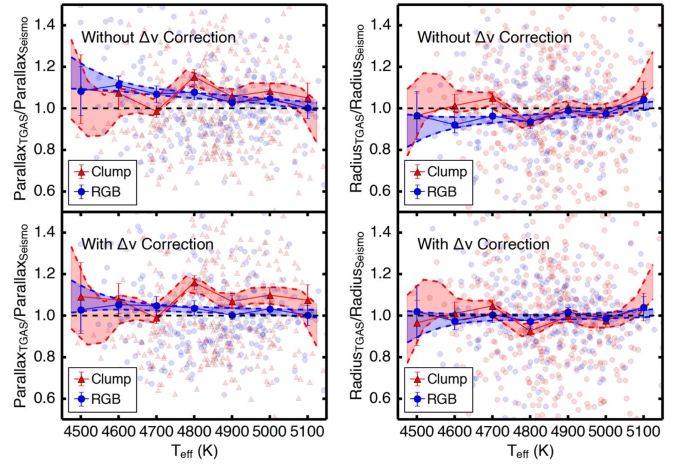

Figure 11. Comparison of parallaxes (left panels) and radii (right panels) for ascending RGB (blue circles) and red clump (red triangles) stars, respectively. Top panels show the comparison without applying a correction to the $\Delta\nu$ scaling relation, while the bottom panels show the comparison with the Sharma et al. (2016) correction applied. Small symbols show the original sample, large symbols with error bars are mean bins, and shaded areas show 68% confidence intervals as in Figure 8.
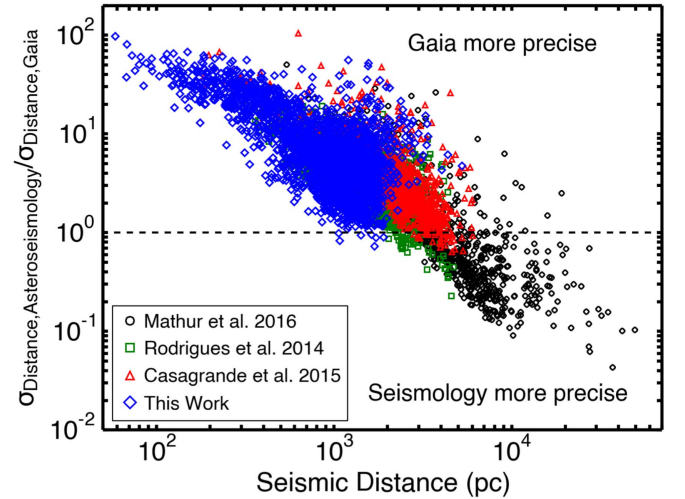

Figure 12. Asteroseismic distance precision divided by the expected end-of-mission *Gaia* uncertainty as a function of seismic distance for different samples of *Kepler* targets. Note that the sample in this work and by Casagrande et al. (2014b) contains dwarfs and giants, while Rodrigues et al. (2014) and Mathur et al. (2016) analyzed giants only.

by TESS (Ricker et al. 2014), red giants in the bulge observed with WFIRST (Gould et al. 2015), and red giants observed with PLATO (Rauer et al. 2014).

5. Conclusions

We presented a detailed comparison of asteroseismic scaling relations with *Gaia* DR1 (TGAS) parallaxes for 2200 *Kepler* stars spanning from the main sequence to the red-giant branch. Our main findings can be summarized as follows.

1. Previously identified offsets between TGAS parallaxes and distances derived from asteroseismology and eclipsing binaries have likely been overestimated for stars beyond 100–200 pc in the *Kepler* field. This implies that

previously proposed TGAS parallax corrections are overestimated for $\pi \lesssim 5 - 10$ mas ($\approx$90%–98% of the TGAS sample). We emphasize that this is most likely due to the larger sample size used here, rather than systematic differences in the methods or distance scales in previous studies. We demonstrate that for subgiants and dwarfs the offsets can be in part compensated by adopting a hotter $T_{\rm eff}$ scale (such as the infrared flux method) as opposed to spectroscopic temperatures. If systematics from scaling relations and TGAS parallaxes are negligible, these results would validate the IRFM as a fundamental $T_{\rm eff}$ scale for dwarfs and subgiants. Residual systematic differences between asteroseismology and TGAS parallaxes are a constant fraction (at the $\approx$2% level) across three orders of magnitude, in line with the previously noted dependence of absolute TGAS parallax offsets with distance.

2. Asteroseismic and *Gaia* radii agree with a residual scatter of $\approx$10% but reveal a systematic offset for subgiants ($\approx$1.5–3 $R_\odot$), with seismic radii being underestimated by $\approx$5%–7%, with a $\approx$2% systematic error depending on the $T_{\rm eff}$ scale. Our results show no significant offsets for main-sequence stars ($\lesssim$1.5 $R_\odot$) and low-luminosity giants with ($R \approx$ 3–8 $R_\odot$), indicating that the offsets derived from eclipsing binaries by Gaulme et al. (2016) do not appear to extend to less evolved stars. Overall, our results demonstrate empirically that systematic errors in radii derived from scaling relations are at or below the $\approx$5% level from $\approx$0.8–10 $R_\odot$.

3. A comparison of parallaxes and radii for RGB and red clump stars shows tentative evidence (at the $\approx 2\sigma$ level) that the $\Delta\nu$ scaling relation correction by Sharma et al. (2016) improves the comparison to *Gaia*. However, the precision of TGAS parallaxes is insufficient to conclusively show whether the $\Delta\nu$ correction is more important for RGB or red clump stars.

4. Our results provide no evidence for systematic errors in asteroseismic scaling relations as a function of metallicity from [Fe/H] ≈ -0.8 to $+0.4$ dex. This provides empirical support for the use of asteroseismology to calibrate spectroscopic pipelines for characterizing exoplanet host stars (e.g., Brewer et al. 2015) and galactic archeology (e.g., Valentini et al. 2017).

5. We used the *Gaia* performance model to predict that asteroseismic distances will remain more precise than *Gaia* end-of-mission data for stars beyond $\approx$3 kpc. This highlights the complementary nature of *Gaia* and asteroseismology for measuring distances to galactic stellar populations.

The study presented here only gives a first glimpse of the powerful synergy between *Gaia* and asteroseismology. In-depth studies using individual frequency modeling using TGAS parallaxes will provide further insights into differences in distance scales and seismic fundamental parameters (e.g., Metcalfe et al. 2017), and new interferometry as well as spectrophotometry for dozens of seismic red giants will provide a more fundamental calibration of the scaling relation for stellar radii. Furthermore, *Gaia* DR2 is expected to provide parallaxes for nearly all $\approx$20,000 oscillating *Kepler* stars (e.g., Mathur et al. 2017), allowing unprecedented scaling relation tests and studies, which can combine frequency modeling and *Gaia* data

to test and improve interior models from the main sequence to the red-giant branch.

Huber et al.

University of Virginia, University of Washington, University of Wisconsin, Vanderbilt University, and Yale University.

References

Amôres, E. B., & Lépine, J. R. D. 2005, AJ, 130, 659
An, D., Beers, T. C., Johnson, J. A., et al. 2013, ApJ, 763, 65
Anders, F., Chiappini, C., Rodrigues, T. S., et al. 2017, A&A, 597, A30
Astraatmadja, T. L., & Bailer-Jones, C. A. L. 2016, ApJ, 832, 137
Bailer-Jones, C. A. L. 2015, PASP, 127, 994
Belkacem, K., Goupil, M. J., Dupret, M. A., et al. 2011, A&A, 530, A142
Bovy, J., Rix, H.-W., Green, G. M., Schlafly, E. F., & Finkbeiner, D. P. 2016, ApJ, 818, 130
Boyajian, T. S., McAlister, H. A., van Belle, G., et al. 2012a, ApJ, 746, 101
Boyajian, T. S., von Braun, K., van Belle, G., et al. 2012b, ApJ, 757, 112
Brewer, J. M., Fischer, D. A., Basu, S., Valenti, J. A., & Piskunov, N. 2015, ApJ, 805, 126
Brown, T. M., Latham, D. W., Everett, M. E., & Esquerdo, G. A. 2011, AJ, 142, 112
Buchhave, L. A., Bizzarro, M., Latham, D. W., et al. 2014, Natur, 509, 593
Buchhave, L. A., & Latham, D. W. 2015, ApJ, 808, 187
Buchhave, L. A., Latham, D. W., Johansen, A., et al. 2012, Natur, 486, 375
Cardelli, J. A., Clayton, G. C., & Mathis, J. S. 1989, ApJ, 345, 245
Casagrande, L., Portinari, L., Glass, I. S., et al. 2014a, MNRAS, 439, 2060
Casagrande, L., Schönrich, R., Asplund, M., et al. 2011, A&A, 530, A138
Casagrande, L., Silva Aguirre, V., Stello, D., et al. 2014b, ApJ, 787, 110
Casagrande, L., & VandenBerg, D. A. 2014, MNRAS, 444, 392
Chaplin, W. J., Elsworth, Y., Davies, G. R., et al. 2014, MNRAS, 445, 946
Chaplin, W. J., & Miglio, A. 2013, ARA&A, 51, 353
Choi, J., Dotter, A., Conroy, C., et al. 2016, ApJ, 823, 102
Christensen-Dalsgaard, J., Kjeldsen, H., Brown, T. M., et al. 2010, ApJL, 713, L164
Davies, G. R., Lund, M. N., Miglio, A., et al. 2017, A&A, 598, L4
De Ridder, J., Molenberghs, G., Eyer, L., & Aerts, C. 2016, A&A, 595, L3
di Mauro, M. P., Cardini, D., Catanzaro, G., et al. 2011, MNRAS, 415, 3783
Dotter, A. 2016, ApJS, 222, 8
Epstein, C. R., Elsworth, Y. P., Johnson, J. A., et al. 2014, ApJL, 785, L28
Frandsen, S., Lehmann, H., Hekker, S., et al. 2013, A&A, 556, A138
Gaia Collaboration, Brown, A. G. A., Vallenari, A., et al. 2016a, A&A, 595, A2
Gaia Collaboration, Prusti, T., de Bruijne, J. H. J., et al. 2016b, A&A, 595, A1
Gaulme, P., McKeever, J., Jackiewicz, J., et al. 2016, ApJ, 832, 121
Gould, A., Huber, D., Penny, M., & Stello, D. 2015, JKAS, 48, 93
Green, G. M., Schlafly, E. F., Finkbeiner, D. P., et al. 2015, ApJ, 810, 25
Grunblatt, S. K., Huber, D., Gaidos, E. J., et al. 2016, AJ, 152, 185
Guggenberger, E., Hekker, S., Basu, S., & Bellinger, E. 2016, MNRAS, 460, 4277
Gustafsson, B., Edvardsson, B., Eriksson, K., et al. 2008, A&A, 486, 951
Hekker, S., Elsworth, Y., De Ridder, J., et al. 2011, A&A, 525, A131
Hekker, S., Elsworth, Y., Mosser, B., et al. 2012, A&A, 544, A90
Hekker, S., Kallinger, T., Baudin, F., et al. 2009, A&A, 506, 465
Holtzman, J. A., Shetrone, M., Johnson, J. A., et al. 2015, AJ, 150, 148
Howell, S. B., Sobeck, C., Haas, M., et al. 2014, PASP, 126, 398
Huang, Y., Liu, X.-W., Yuan, H.-B., et al. 2015, MNRAS, 454, 2863
Huber, D. 2015, in Giants of Eclipse: The Zeta Aurigae Stars and Other Binary Systems (Cham: Springer International), 169
Huber, D. 2016, arXiv:1604.07442
Huber, D. 2017, isoclassify: v1.2, Zenodo, doi:10.5281/zenodo.573372
Huber, D., Bedding, T. R., Arentoft, T., et al. 2011, ApJ, 731, 94
Huber, D., Carter, J. A., Barbieri, M., et al. 2013a, Sci, 342, 331
Huber, D., Chaplin, W. J., Christensen-Dalsgaard, J., et al. 2013b, ApJ, 767, 127
Huber, D., Ireland, M. J., Bedding, T. R., et al. 2012, MNRAS, 423, L16
Huber, D., Stello, D., Bedding, T. R., et al. 2009, CoAst, 160, 74
Jao, W.-C., Henry, T. J., Riedel, A. R., et al. 2016, ApJL, 832, L18
Johnson, J. A., Huber, D., Boyajian, T., et al. 2014, ApJ, 794, 15
Jordi, C., Gebran, M., Carrasco, J. M., et al. 2010, A&A, 523, A48
Jordi, K., Grebel, E. K., & Ammon, K. 2006, A&A, 460, 339
Kjeldsen, H., & Bedding, T. R. 1995, A&A, 293, 87
Kurucz, R. L. 1993, SYNTHE Spectrum Synthesis Programs and Line Data (Cambridge, MA: Smithsonian Astrophysical Observatory)
Lindegren, L., Lammers, U., Bastian, U., et al. 2016, A&A, 595, A4
Mathur, S., García, R. A., Huber, D., et al. 2016, ApJ, 827, 50
Mathur, S., Huber, D., Batalha, N. M., et al. 2017, ApJS, 229, 30
Metcalfe, T., Creevey, O., & van Saders, J. 2017, arXiv:1701.08746
Miglio, A., Brogaard, K., Stello, D., et al. 2012, MNRAS, 419, 2077
Miglio, A., Chaplin, W. J., Brogaard, K., et al. 2016, MNRAS, 461, 760
Miglio, A., Montalbán, J., Baudin, F., et al. 2009, A&A, 503, L21
Miglio, A. 2012, in Red Giants as Probes of the Structure and Evolution of the Milky Way, Astrophysics and Space Science Proceedings, ed. A. Miglio, J. Montalbán, & A. Noels (Berlin: Springer), 11
Mosser, B., & Appourchaux, T. 2009, A&A, 508, 877
Mosser, B., Michel, E., Belkacem, K., et al. 2013, A&A, 550, A126
Paxton, B., Bildsten, L., Dotter, A., et al. 2011, ApJS, 192, 3
Paxton, B., Cantiello, M., Arras, P., et al. 2013, ApJS, 208, 4
Paxton, B., Marchant, P., Schwab, J., et al. 2015, ApJS, 220, 15
Petigura, E. 2015, PhD thesis, Univ. California (arXiv:1510.03902)
Pinsonneault, M. H., An, D., Molenda-Żakowicz, J., et al. 2012, ApJS, 199, 30
Pinsonneault, M. H., Elsworth, Y., Epstein, C., et al. 2014, ApJS, 215, 19
Rauer, H., Catala, C., Aerts, C., et al. 2014, ExA, 38, 249
Ricker, G. R., Winn, J. N., Vanderspek, R., et al. 2014, Proc. SPIE, 9143, 20
Rodrigues, T. S., Girardi, L., Miglio, A., et al. 2014, MNRAS, 445, 2758
SDSS Collaboration, Albareti, F. D., Allende Prieto, C., et al. 2016, ApJS, submitted (arXiv:1608.02013)
Serenelli, A. M., Bergemann, M., Ruchti, G., & Casagrande, L. 2013, MNRAS, 429, 3645
Sesar, B., Fouesneau, M., Price-Whelan, A. M., et al. 2017, ApJ, 838, 107
Sharma, S., Stello, D., Bland-Hawthorn, J., Huber, D., & Bedding, T. R. 2016, ApJ, 822, 15
Sharma, S., Stello, D., Huber, D., Bland-Hawthorn, J., & Bedding, T. R. 2017, ApJ, 835, 163
Silva Aguirre, V., Casagrande, L., Basu, S., et al. 2012, ApJ, 757, 99
Silva Aguirre, V., Davies, G. R., Basu, S., et al. 2015, MNRAS, 452, 2127
Silva Aguirre, V., Lund, M. N., Antia, H. M., et al. 2017, ApJ, 835, 173
Stassun, K. G., & Torres, G. 2016a, AJ, 152, 180
Stassun, K. G., & Torres, G. 2016b, ApJL, 831, L6
Stello, D., Chaplin, W. J., Basu, S., Elsworth, Y., & Bedding, T. R. 2009, MNRAS, 400, L80
Stello, D., Huber, D., Bedding, T. R., et al. 2013, ApJL, 765, L41
Stello, D., Vanderburg, A., Casagrande, L., et al. 2016, ApJ, 832, 133
Stello, D., Zinn, J., Elsworth, Y., et al. 2017, ApJ, 835, 83
Torres, G., Fischer, D. A., Sozzetti, A., et al. 2012, ApJ, 757, 161
Valentini, M., Chiappini, C., Davies, G. R., et al. 2017, A&A, 600, A66
Verner, G. A., Elsworth, Y., Chaplin, W. J., et al. 2011, MNRAS, 415, 3539
Vrard, M., Mosser, B., & Samadi, R. 2016, A&A, 588, A87
Wang, L., Wang, W., Wu, Y., et al. 2016, AJ, 152, 6
White, T. R., Bedding, T. R., Stello, D., et al. 2011, ApJ, 743, 161
White, T. R., Huber, D., Maestro, V., et al. 2013, MNRAS, 433, 1262
Zinn, J. C., Huber, D., Pinsonneault, M. H., & Stello, D. 2017, ApJ, in press (arXiv:1706.09416)